Journal of Materials Chemistry A

ROYAL SOCIETY OF CHEMISTRY

PAPER

View Article Online
View Journal

Cite this: DOI: 10.1039/d6ta00653a

Control of ion exchange capacity in block copolymer binders enables high hydroxide conductivity at low swelling and improves catalyst activity for AEM water electrolysis

Richard Weber,[a] Malte Klingenhof,[b] Oleksandr Dolynchuk,[c] Luis Hagner,[de] Lukas Metzler,[de] Susanne Koch,[de] Mario Zerson,[ag] Robert Magerle,[ag] Peter Strasser,[b] Severin Vierrath[de] and Michael Sommer *[af]

The development of membranes for anion exchange membrane water electrolysis (AEMWE) has recently been extremely fruitful, but less effort has been devoted to specific tailoring of polymeric binders to enhance catalyst utilization and electrical conductivity within the catalyst layer. Herein we report a simple one-pot synthesis of block copolymers (BCP) for application as anode binders in AEMWE. The BCPs contain hydrophilic poly(biphenyl piperidinium) and hydrophobic blocks based on *meta*-terphenyl and 2,2,2-trifluoroacetophenone of varying fractions. The synthetic approach provides facile access to ionomers with largely varied ion exchange capacities (IECs) between 0.94 and 2.68 meq. g^{-1}, giving rise to binders with extremely low swelling yet efficient hydroxide transport. The least hydrophilic BCP with ~25 wt-% hydrophilic fraction and an IEC of 0.94 meq. g^{-1} exhibits a high hydroxide conductivity of σ_{OH} = 174 mS cm^{-1} at 80 °C at a low water uptake of 13% at 80 °C, and almost temperature-independent swelling. The low water uptake enables increased catalyst utilization in nickel-iron layered double-hydroxide-based anodes, which, in combination with the high hydroxide conductivity, results in an improved AEMWE performance. AEMWE single cells exhibit current densities of 3800 mA cm^{-2} at 2 V, not achieved neither by using statistical copolymer analogs nor commercial-type binders.

Received 23rd January 2026
Accepted 14th May 2026

DOI: 10.1039/d6ta00653a

rsc.li/materials-a

Introduction

Anion-exchange membrane water electrolysis (AEMWE) is key for green hydrogen production combining the advantages of conventional alkaline electrolysis and proton-exchange membrane water electrolysis (PEMWE).[1,2] The zero-gap configuration and the possibility of using non-precious metal catalysts renders this technology cost-effective whilst providing operation at high current densities.[3,4] Within an AEM water electrolyser, the membrane electrode assembly (MEA) is the key component for separating the half cells, conducting hydroxide ions and catalyzing water electrolysis. It consists of an anion-exchange membrane which is coated with conductive carbon and catalyst particles immobilized by an ion-conducting binder polymer.[5–8] Reported binder polymers include polyethylene,[9,10] polystyrene,[11,12] polysulfones,[13–16] polyphenylene oxides,[17,18] polybenzimidazoles,[19,20] poly(arylene alkylene)s,[21–24] Nafion[25,26] or polytetrafluoroethylene.[26–28] For high performance and long-term operational stability of the AEM electrolyzer, the binder polymer must fulfill a broad range of criteria, among them chemical stability and suitable gas transport properties.[3,8,12,29,30] Chemical stability includes alkaline and electrochemical stability, which are strong demands under caustic and oxidizing operating conditions in close proximity to catalytically active sites.[12,21,29] For example, in an effort to improve the long-term stability of AEM devices, the adsorption tendency of aromatic binder polymers on Pt/C catalysts has been reduced to suppress phenyl oxidation.[31]

The role of the binder to help form an optimal MEA morphology is also key for ideal catalyst utilization within the so-called triple-phase-boundary.[5,32,33] Here, a low water uptake (WU) and a low swelling is beneficial to maintain contact of catalyst particles and hence improve electrical conductivity

[a]*Institute of Chemistry, Chemnitz University of Technology, Straße der Nationen 62, 09111 Chemnitz, Germany. E-mail: michael.sommer@chemie.tu-chemnitz.de*
[b]*Department of Chemistry, Technical University Berlin, Straße des 17. Juni 124, 10623 Berlin, Germany*
[c]*Institute of Physics, Martin Luther University Halle-Wittenberg, Van-Danckelmann-Platz 3, 06120 Halle, Germany*
[d]*Electrochemical Energy Systems, IMTEK-Department of Microsystems Engineering, University of Freiburg, Georges-Koehler-Allee 103, 79110 Freiburg, Germany*
[e]*Hahn-Schickard, Georges-Koehler-Allee 103, 79110 Freiburg, Germany*
[f]*Research Center for Materials, Architectures and Integration of Nanomembranes (MAIN), Chemnitz University of Technology, Rosenbergstr. 6, 09126 Chemnitz, Germany*
[g]*Institute of Physics, Chemnitz University of Technology, Reichenhainer Straße 70, 09126 Chemnitz, Germany*

within the catalyst layer.[34] A low swelling has also been reported to improve the stability of AEM electrolyzers.[20] Similarly, for quaternized polystyrene ionomers a high IEC of the binder is of disadvantage for long-term operation of AEMWE, since catalyst particles may detach from the MEA.[11] Somewhat in contrast, we previously found that within a series of poly(terphenyl piperidinium)s used as binders, an increasing WU led to higher hydroxide conductivities, catalyst utilization and improved AEMWE single cell performance.[35] This emphasizes the necessity for a more profound understanding of the interplay of the diverse functions of the ionomer binder that contribute to AEMWE performance and stability.

Strategies to tune, control and limit swelling of AEMWE materials are manifold, and have mostly been reported in the context of membranes rather than binders. These include, but are not limited to, reinforcements,[36] fluorination,[37] branching,[38] multi-cationic side-chains[39] or crosslinking.[40] Similarly, by virtue of phase-separation of block copolymers (BCP) or segmented architectures in general, hydrophilic, ion-containing segments may segregate into domains of high charge density to optimize ion transport. Eventually, the remaining compartments may be tailored to meet further criteria such as mechanical strength or gas permeation. BCPs with cationic groups can be prepared by *e.g.* ring-opening metathesis polymerization,[41] radical polymerization,[42] polyinsertion[10,43] or polyhydroxyalkylation.[42,44] To name examples, BCPs prepared by atom-transfer radical polymerization showed a WU of 123% at 80 °C and a hydroxide conductivity ($\sigma_{OH,80}$) of 81 mS cm^{-1} at 80 °C.[42] Pentablock polynorbornenes made *via* vinyl addition polymerization reached a WU of 85% at 25 °C and a $\sigma_{OH,80}$ of 100 mS cm^{-1} at 80 °C.[43] Using polyhydroxyalkylation, poly(-biphenyl alkylene) *block* copolymers with ammonium side-chains delivered a σ_{OH} of 162 mS cm^{-1} at 108% WU and 80 °C, and were deployed as membranes and binders simultaneously.[44] However, dedicated studies aiming to vary and understand binder properties are much less prevalent compared to the large body of literature available on membranes. Considering the key role of the binder for optimizing morphology of the triple-phase-boundary, BCPs appear highly promising.

Herein, we report a simple one-pot synthesis of block copolymers *via* polyhydroxyalkylation for application as anode binder ionomers in AEMWE and compared their performance with statistical copolymer analogs of identical composition. Varying the ratio between the hydrophilic poly(biphenyl piperidinium) (PBP) block and the hydrophobic block based on *meta*-terphenyl and 2,2,2-trifluoroacetophenone yields BCPs with largely varied ion exchange capacity (IEC), and thus swelling properties. The hydrolytic stability of the BCP binders increased with increasing IEC as a result of the increased nucleophilicity of the hydroxide anion under low hydration conditions. The BCP with ~25 wt-% hydrophilic fraction exhibited a high hydroxide conductivity (σ_{OH} = 174 mS cm^{-1}) at very low IEC (0.94 meq. g^{-1}) and thus low hydration (WU = 13%), leading to superb binder capability when used as binder in nickel-iron layered double-hydroxide (NiFe-LDH)- based anodes. A binder pre-screening *via* rotating disk electrode (RDE) experiments correlated well with AEMWE single cell testing, revealing that the low IEC binder outperforms all other BCPs, statistical as well as commercial-type poly(arylene piperidinium) analogs. Current densities of 3800 mA cm^{-2} at 2 V were obtained in AEMWE single cell tests with the best BCP, which is approx. 1000 mA cm^{-2} higher compared to commercial PiperION-A. This improvement in performance is explained by the synergistic effect of the low IEC enabling enhanced catalyst utilization as a result of a better electrical conductivity within the catalyst layer, combined with a simultaneously improved hydroxide conductivity.

Results and discussion

The block copolymers were synthesized by superacid-catalyzed *Friedel-Crafts*-type polyhydroxyalkylation and subsequent quaternization with methyl iodide.[45] The synthetic strategy towards the BCPs is based on a hydrophilic segment consisting of biphenyl (BP) and *N*-methyl-4-piperidone (Pip), leading to a large IEC of 3.56 meq. g^{-1}. The hydrophobic segment was made from *meta*-terphenyl (*m*TP) and 2,2,2-trifluoroacetophenone (TFAp). The *m*TP monomers lead to kinked segments which support microphase separation as a result of an increased chain flexibility.[46,47] Block copolymers were prepared by the sequential addition of monomers (Scheme 1a). First, trifluoromethanesulfonic acid (TFSA) and trifluoroacetic acid (TFA) were added to a mixture of BP and Pip to form the hydrophilic segment. Since the ketone to arene ratio was 0.95, the molar masses resulted in a plateau value with no further growth of the chains as monitored *via* size exclusion chromatography (SEC, see Fig. S1). We assumed that the small excess of arene led to BP-terminated hydrophilic starting blocks, which is confirmed by MALDI-ToF data (Figure S2). The number average

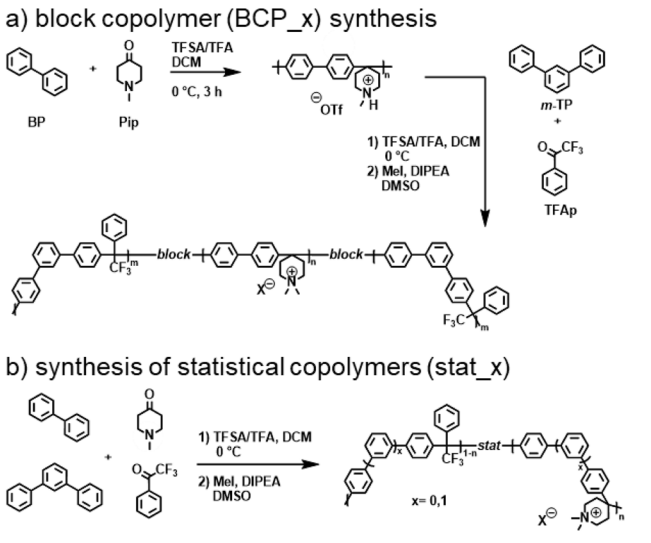

Scheme 1 Synthesis of (a) block copolymers and (b) statistical copolymers based on biphenyl, *N*-methylpiperidone, *meta*-terphenyl and 2,2,2- trifluoroacetophenone (trifluoromethanesulfonic acid (TFSA), trifluoroacetic acid (TFA), dichloromethane (DCM), *N,N*-di-*iso*propylethylamine (DIPEA), dimethylsulfoxide (DMSO)).

Table 1 Molar masses and dispersities from size exclusion chromatography after polystyrene calibration, composition and ion exchange capacities (IEC) of the investigated block and statistical copolymers as theoretical (th) and experimentally titrated (titr) values

Polymer	M_n/kg mol^{-1}	M_w/kg mol^{-1}	$Đ$	wt% hydrophilic	IEC$_{th}$ (Cl$^-$)/meq. g^{-1}	IEC$_{th}$ (OH$^-$)/meq. g^{-1}	IEC$_{titr}$ (Cl$^-$)/meq. g^{-1}
BCP_79	24	71	3.0	79	2.68	2.82	2.34
stat_73	57	177	3.1	73	2.48	2.61	2.50
BCP_55	37	88	2.4	55	1.90	1.97	1.85
stat_46	30	72	2.4	46	1.59	1.64	1.54
BCP_26	39	98	2.5	26	0.92	0.94	0.71
stat_22	34	57	1.7	22	0.77	0.79	0.97

molecular weights and dispersities of the hydrophilic starting blocks from SEC and calibration with polystyrene standards were $M_{n,SEC}$ = 4.1–4.5 kg mol^{-1} and $Đ$ = 1.6–1.7, respectively. *m*TP and TFAp as well as TFSA/TFA were subsequently added to the reaction mixture to grow the hydrophobic blocks. The segment length of the hydrophobic blocks was controlled by the amount of hydrophobic monomers, finally resulting in different weight fractions of the hydrophilic block and thus IECs. At this point we assume that a triblock copolymer structure forms due to the reactive biphenyl end groups at both sides of the hydrophilic starting block. However, multiblock copolymer architectures are possible as well upon depending on the probability of the hydrophobic block reacting at either chain end as well. We assume this probability to mostly depend on the concentration of hydrophobic monomers and thus on their weight fraction. To what extent tri- and multiblock copolymers coexist is unclear due to the difficulties of analytical identification. As reference materials, statistical copolymers were prepared by mixing all monomers in the beginning of the reaction in the same ratios (Scheme 1b). The polymers were denoted as BCP_x and stat_*x*, where *x* denotes the weight fraction of hydrophilic segments with hydroxide acting as counter ion.

The number and weight average molar weights and dispersities determined *via* SEC are compiled in Table 1. All final copolymers were purified *via* Soxhlet extraction with methanol and subsequently acetone to remove oligomers and yield comparable molar masses. Fig. S3 monitors the success of Soxhlet extraction. Fig. 1 shows the SEC curves of the three individually prepared hydrophilic starting blocks of almost identical molar masses ($M_{n,SEC}$ = 4.1–4.5 kg mol^{-1}) together with the corresponding final BCP products. All chromatograms of the BCPs were shifted towards lower elution volumes with vanishing intensity in the region of the starting block, which confirms the success of the synthetic strategy. The ^{1}H NMR spectra of the BCPs further proved the presence of both hydrophilic and hydrophobic segments, confirming a successful linkage of hydrophilic and hydrophobic blocks (Figures S4–5). The IECs and compositions were determined *via* ^{1}H NMR spectroscopy as well as from titration (Table 1).

To study the bulk morphology of the prepared ionomers, small-angle (SAXS) and wide-angle X-ray scattering (WAXS) experiments were performed on dry (with iodide as counter ion) as well as on wet polymers (hydroxide form) (Fig. 2). In the dry state, BCP_26 and BCP_55, but not BCP_74, showed a very broad and weak SAXS scattering intensity in the 0.03 Å^{-1} < q <

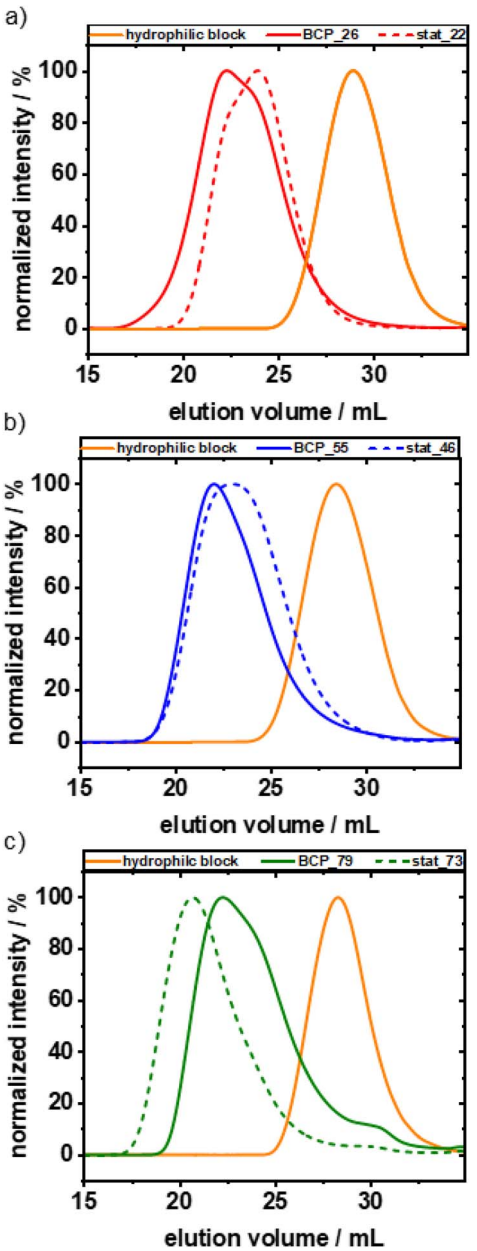

Fig. 1 SEC curves of hydrophilic starting blocks, final block copolymers after purification and statistical analogs: BCP_26, stat_22 (a), BCP_55, stat_48 (b), BCP_79, stat_73 (c). SEC curves were measured at 70 °C in DMF containing ammonium trifluoroacetate (0.1 M) at a flow rate of 1 mL min^{-1} and calibrated against PS standards.

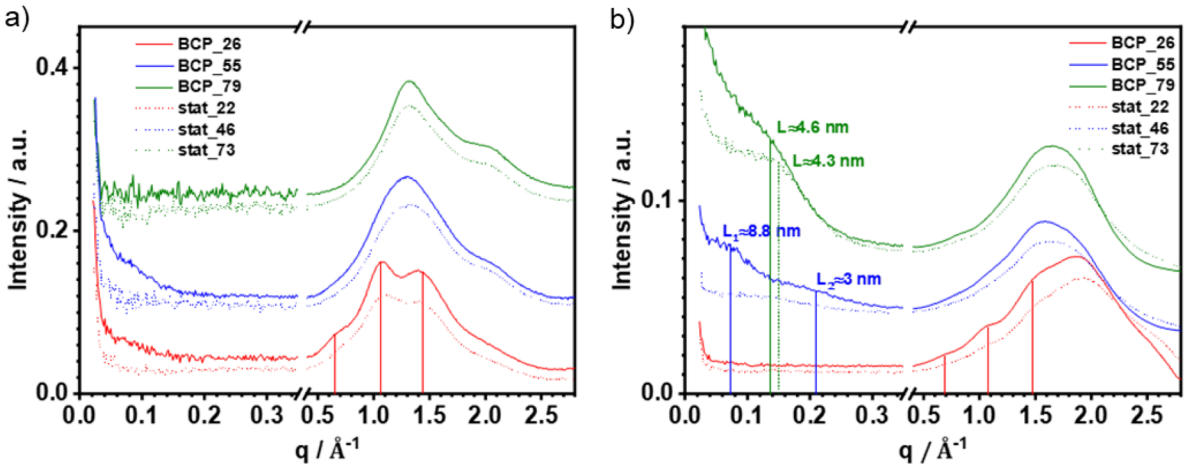

Fig. 2 SAXS and WAXS patterns of (a) dry polymers in iodide form and (b) polymers after water uptake (hydroxide form). The curves are shifted vertically for clarity.

0.2 $Å^{-1}$ region. This corresponds to density variations on length scales of 3 to 20 nm without long-range order (Fig. 2a). The broad distribution of SAXS intensity that is also clearly seen in a double-log plot is a clear difference compared to the statistical polymers that did not show any scattering intensity in the same region (Fig. S6). The WAXS pattern of BCP_26 featured three additional peaks (red lines in Fig. 2a) that resemble those of the corresponding hydrophobic homopolymer (see Fig. S7). These WAXS peaks were not visible in the patterns of the less hydrophobic BCP_55 and BCP_79 and indicated the ability of the hydrophobic block to order on a length scale of ~1 nm. The WAXS pattern of the dry stat_22, however, showed these same peaks, albeit with lower intensity. This indicates that the distribution of monomers in the statistical copolymer is not entirely random, but segmented to some extent. To underline this hypothesis further, we investigated the development of molecular weight of the four possible homopolymers with time. For the combination of BP and Pip, the increase in molecular weight was strongest due to the larger electrophilicity of *N*-pip compared to TFAp and the higher reactivity of BP compared to *m*TP, corroborating the idea of segmentation (Fig. S8). This would allow segments similar to the hydrophilic starting blocks used for BCP synthesis to form.

The SAXS curves of the wet block copolymers showed distinct changes upon water uptake (Fig. 2b). While BCP_55 and BCP_79 showed an increase in scattering intensity with increasing fraction of the hydrophilic block, the broad and weak peaks of the dry BCP_26 vanished. For BCP_79, a *d*-spacing of 4.6 nm was observed. For BCP_55, two SAXS peaks corresponding to *d*-spacings of 8.8 and 3 nm were found, *i.e.* the long period of BCP_55 shifted to lower *q* values compared to the dry sample. Such humidity-dependent swelling and corresponding shifting of SAXS "ionomer" peaks to lower *q* values is well known for proton conducting membranes and indicates clustering of hydrophilic parts of the chain with water.[48,49]

The vanishing SAXS peak of the wet BCP_26 is not surprising considering that the rather irregular, poorly ordered structure of the dry sample may become even less regular upon swelling. The fact that the three WAXS peaks of wet BCP_26 were retained to some extent indicates that the order of the hydrophobic part is preserved upon swelling (note that the different overall shapes of the WAXS patterns of the dry and wet samples are caused by the different measurement conditions, the use of a sealed glass capillary, and the presence of water).

Compared to the BCPs, the SAXS curves of the hydrated membranes made from the statistical copolymers were qualitatively similar, albeit showing less defined peaks. Also here, the scattering intensity increased with increasing water content. For stat_46 and stat_74 two broad peaks were observed corresponding to the characteristic distances of 4.7 and 4.3 nm, respectively.

Compared to classical BCP self-assembly,[50] the herein made BCP samples show poor order on the 3 to 20 nm length scale. This is not surprising considering their large dispersities (see Table 1) as well as the fact that with decreasing hydrophobic fraction, the probability for the formation of multiblock architectures increases. Furthermore, it is possible that monomer scrambling occurs during the synthesis of the second block as a result of transalkylation,[51] *i.e.* as soon as the mixture of *m*TP and TFAp is added. Although the molar mass of the hydrophilic block was shown to be stable in the absence of the second portion of hydrophobic monomers (*c.f.* Fig. S1), such fragmentation process would decrease the initially formed hydrophilic block length leading to a reduced tendency for phase separation. To this end, a model experiment was conducted in which an excess of BP was added to a freshly grown hydrophilic block, resulting in a decrease of $M_{n,SEC}$ from 22 to 17 kg mol^{-1} within 2 h (Fig. S9). Thus, monomer scrambling seems possible upon addition of *m*TP and TFAp under acidic conditions. However, to what extent such process has been present during the synthesis of BCP_26 cannot be probed directly, and so the correlation of redistributed hydrophilic and hydrophobic monomers in the chain with the absence of a SAXS peak remains to be proven. If present, the resulting segment distribution is governed by the

mechanism of the polyhydroxylation reaction, and the morphologies of the final BCP products would certainly be influenced.

Overall, the processes of segmentation of statistical copolymers and possibly fragmentation of the first block during the synthesis of the second cause a rather complex chain sequence and render full control over chain architecture challenging. While clear differences in the phase behavior of the BCP and stat samples remain, we note that these two processes could finally lead to more similar chain sequences than anticipated. To further characterize the nanomorphology of the membranes, thin BCP films were imaged with atomic force microscopy (AFM) in the dry state (Fig. 3a–c). BCP_26 exhibited a terrace-like surface topography, with a step height of approximately 2–2.5 nm between the terraces. In contrast, BCP_55 and BCP_79 showed a smooth surface with fine granular domains. The broad SAXS scattering intensity of dry BCP_55 and BCP_79 indicated density variations on length scales of 3 to 20 nm without long-range order (Fig. 2a). This is consistent with the fine-grained morphology of the thin film surface of these samples. To obtain information on the phase separation of two homopolymers in general, a μm thick blend film was prepared (25 wt-% hydrophilic PBP and 75 wt-% poly(*meta*-terphenyl 2,2,2-trifluoroacetophenone), P*m*TPTFAp). This film showed large, spherical domains of P*m*TPTFAp of up to 200 μm embedded in a matrix of PBP (Fig. 3d). This is a clear indication for a rather strong tendency of the two homopolymers to phase separate. Visually, the homopolymer blend film appeared turbid, while the BCP films were fully transparent. This is consistent with the domain sizes observed using SAXS, AFM and optical microscopy (Fig. 3e and f).

The water uptake (WU) and swelling behavior of the BCPs was investigated and compared to the statistical copolymers. Fig. 4 shows the WU, hydration numbers, through-plane swelling ratio and areal swelling, as a function of temperature. The WU and hydration numbers (λ) were governed by the fraction of the hydrophilic block. WU further increased with temperature for all samples, with an increase that was stronger with higher IEC (Fig. 4a and b).

The swelling ratio (SR) for BCP_26 and stat_22 remained at a similarly low level and was mostly independent of temperature (Fig. 4c and d). Furthermore, the higher the IEC, the stronger WU and λ were increasing. The BCPs span a broad range of WU values, with BCP_79 and BCP_26 exhibiting the highest and lowest water uptake of 92% and 13% at 80 °C, respectively. The statistical copolymers behaved similarly, with

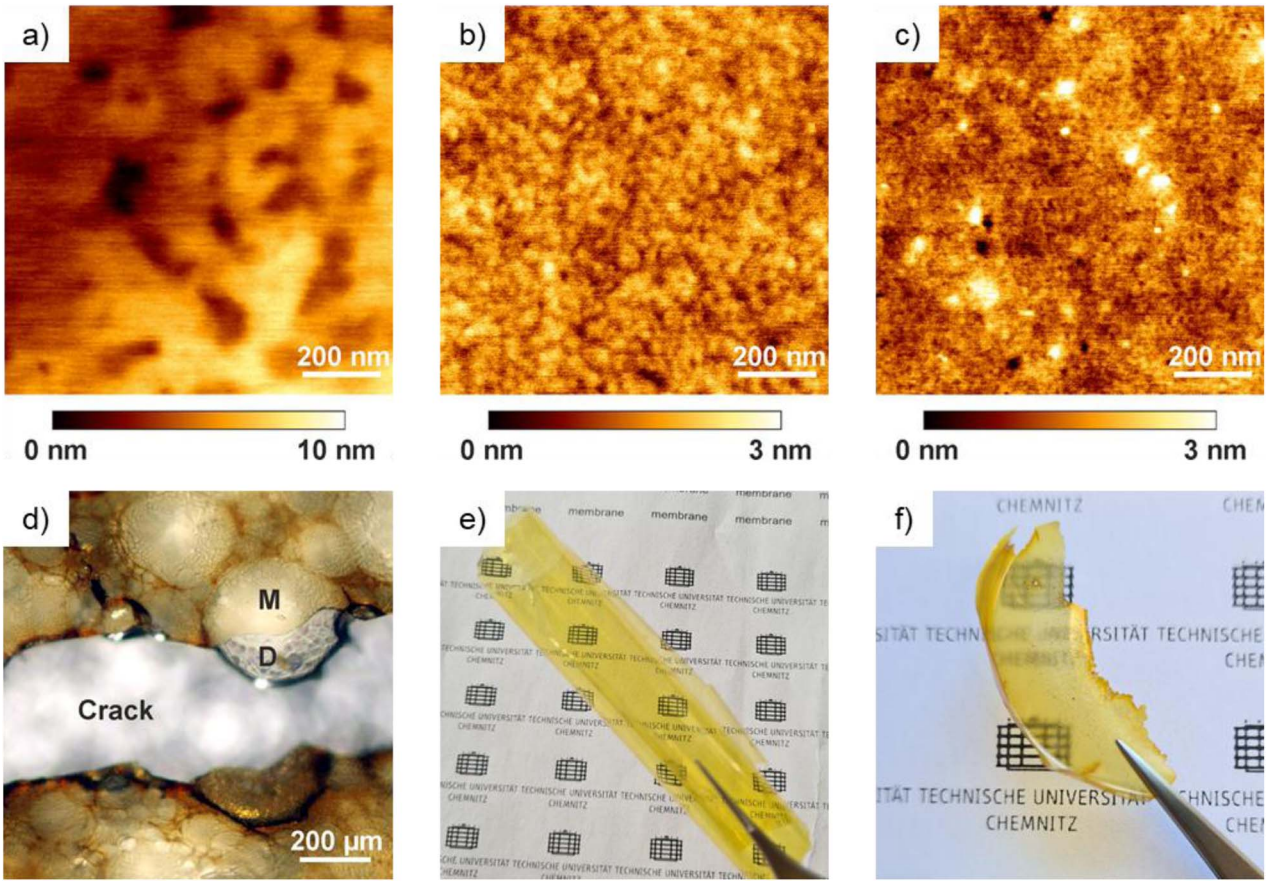

Fig. 3 AFM height images of BCP films: (a) BCP_26, (b) BCP_55, (c) BCP_79. (d) Optical microscopy image of a homopolymer blend forming PTT domains embedded in a PBP matrix. At a crack, the breakout of a large domain (D) of P*m*TPTFAp from the PBP matrix (M) is clearly visible. Visual appearance of BCP_26 (e) and the investigated homopolymer blend (f).

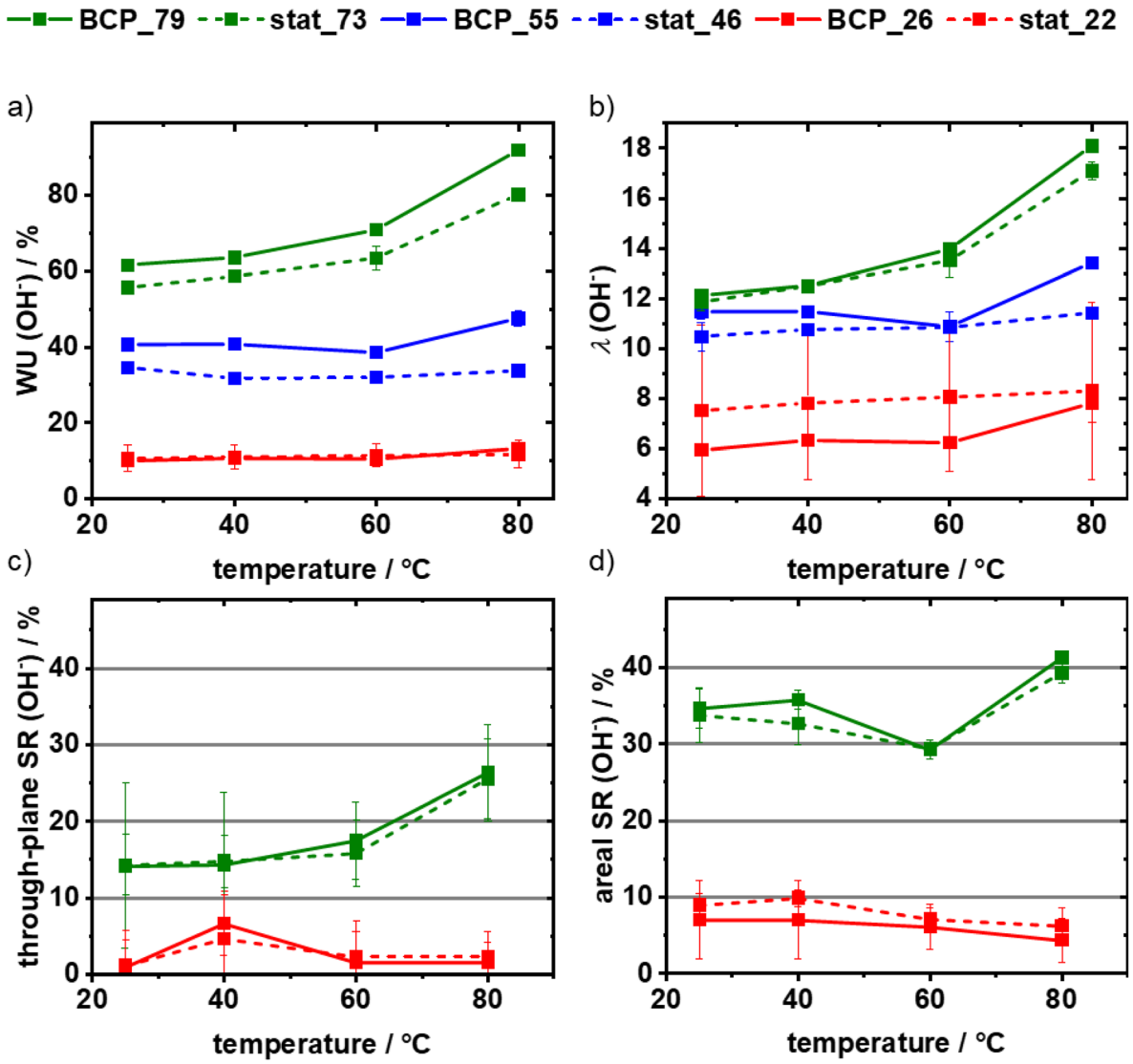

Fig. 4 Water uptake WU (a), hydration number λ (b), through-plane (c) and areal swelling ratio (d) of the block *versus* statistical copolymer.

notable differences in WU and λ resulting from slightly varied composition compared to the BCPs as well as from the assumed similar monomer distribution. The temperature-independent swelling behavior of BCP_26 and stat_22 renders them ideal for binder applications since minimal tension is expected in the catalyst layer upon changing conditions. We anticipate the low WU and the temperature-independent swelling of BCP_26 to stem from both the small weight fraction of the hydrophilic block as well as from the ability of the hydrophobic block to retain order also in the hydrated state (see WAXS pattern in Fig. 2). Fig. 5a and b depict temperature-dependent (Fig. 5a) and hydration number-dependent (Fig. 5b) hydroxide conductivities. In all cases, the conductivities increased with temperature in a similar manner. Due to the temperature-dependent conductivity but temperature-independent water uptake of BCP_26, the conductivity *versus* hydration number plot was rather steep (Fig. 5b), such that a small change in hydration caused a large change in hydroxide conductivity. The activation energies (E_a) of hydroxide transport are given in Table S1. With increasing IEC, the E_a of the statistical copolymers decreases. The same is observed in case of the BCPs except for BCP_26, which shows a significantly lower E_a than stat_22. This supports the observation of better-connected ion transport channels. BCP_79 and stat_73 reached similarly high hydroxide conductivities at 80 °C but required substantially larger amounts of water and accordingly swelled much stronger. The BCP and stat samples with balanced hydrophilic/hydrophobic fractions showed the lowest values of hydroxide conductivity (76 mS cm^{-1}). The highest hydroxide conductivity of 174 mS cm^{-1} was measured for BCP_26 at 80 °C. This is remarkable considering that this sample featured the lowest IEC (0.94) and the lowest WU (13%) of all BCP samples, suggesting potential use in membrane applications also. When normalizing σ (OH^-) by IEC (Figure S10), BCP_26 showed again the highest ion conductivity, confirming the benefit of the block copolymer architecture in terms of phase separation and ionic transport.

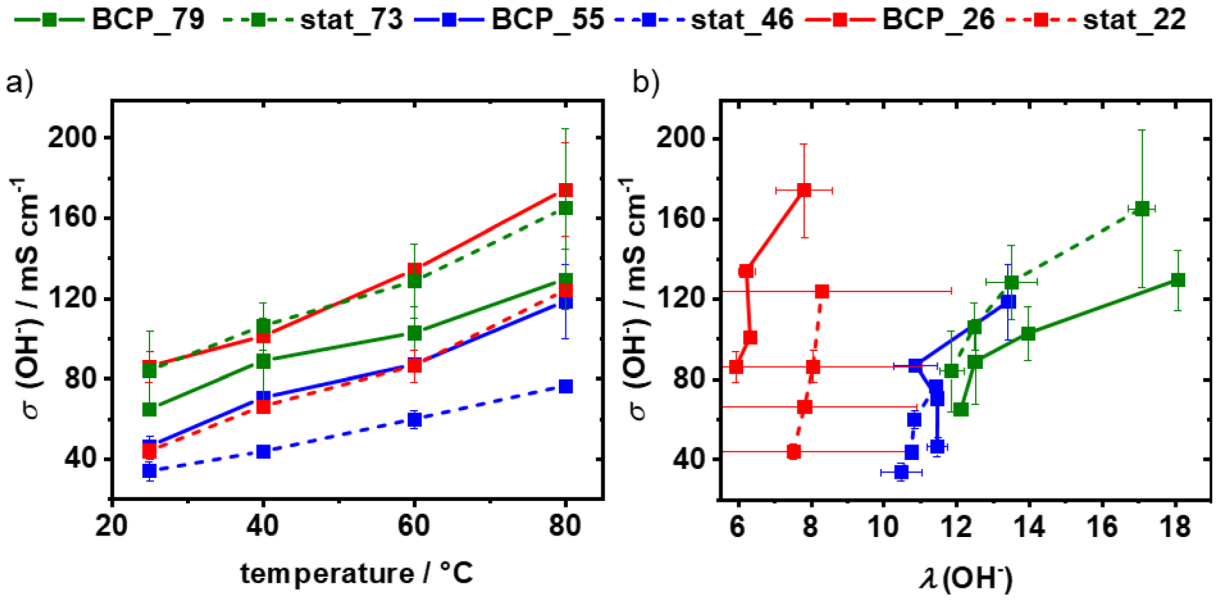

Fig. 5 Hydroxide conductivity depending on temperature (a) and hydration number (b) of the investigated copolymers.

It is also remarkable that BCP_26 exhibits similar SAXS (Fig. 2a and c) and temperature-dependent WU behavior (Fig. 4a) compared to the statistical sample stat_22, but a significantly higher hydroxide conductivity at lower hydration values. While the presence of a SAXS peaks is often considered a necessary prerequisite for a material to exhibit a beneficial morphology for ion transport,[42,52] the different conductivity behavior of BCP_26 and stat_22 may reflect subtle morphological differences not captured by the herein used scattering techniques.

The hydrolytic stability of all copolymers was evaluated in membrane form in 2 M NaOH at 90 °C (Fig. S11–S14), and followed by ^{1}H NMR spectroscopic analysis.[24] An increasing IEC correlated with an increasing hydrolytic stability of the piperidinium cation, along with the known degradation pathways of quaternary ammonium groups in alkaline media. It is interesting to note that a lower IEC strongly reduced stability, as a result of the higher nucleophilicity of the hydroxide anion under low hydration conditions.[53] For the future use of low IEC binders, hydrolytically more stable cations other than dimethyl piperidinium should be incorporated.[54–59]

To evaluate the potential of the BCPs to act as binders in catalyst anode layers for the oxygen evolution reaction (OER), rotating disk electrode (RDE) experiments were conducted (Fig. 6). Disk electrodes were prepared from all BCP samples and referenced against the three analogous statistical copolymers as well as further statistical, literature-known copolymers consisting of *m*TP, *para*-terphenyl (*p*TP), Pip and TFAp, hereafter referred to as M0 (self-made PiperION-A) and M100 (analog with 100% *m*TP instead of *p*TP). These two polymers have been previously studied as binders, with M100 yielding significantly enhanced performance under similar conditions.[35] As a non-precious metal catalyst, nickel iron layered double hydroxides (NiFe-LDH) was used.[35] RDE measurements were conducted in 0.1 M KOH solution at room temperature and a rotation rate of 1600 rpm. Fig. 6a and b clearly show that the ionomers with the lowest hydrophilicity exhibited the best OER performance. An increasing hydrophilicity decreased the OER performance for all copolymers. However, not only BCP_26 showed high OER activity. Also, stat_22 as binder gave an OER activity of almost the same level. The fact that stat_22 exhibited a substantially lower hydroxide conductivity indicates this was not the prime factor determining RDE performance. This assumption is further confirmed by the performance of BCP_55 and BCP_79, which had reversed trends of conductivity and current density. To further evaluate the stability of the disk electrodes, the RDE performance was also studied after 25 cyclic voltammograms (Fig. 6c–e). A significant loss of performance was only observed for all copolymers with low initial RDE performance. This decrease is explained by microbubble formation where the catalytically active sites are blocked by oxygen due to limited escape of the product gas.[60]

The enhancement of reaction kinetics and cycling stability seems to be strongly related to the IEC and the WU of the ionomer binder. This is also visible from the strong oxidation peak around 1.45 V when using BCP_26 and BCP_55 as binders (Fig. 6a). While the large WU of BCP_74 likely separates the catalyst particles, BCP_26 and stat_22 binders allow for sufficient electrical contact, causing a more pronounced oxidizing peak at 1.45 V and hence higher current densities. Thus, we find a strong correlation of RDE performance with IEC, WU and swelling, but not hydroxide conductivity, such that lowering WU increases current density. We rationalize this result by assuming that low IEC binders that are less hydrated improve contact of catalyst particles and electrical conductivity of the catalyst layer, ultimately leading to enhanced catalyst utilization. Similar effects have been reported for Pt/carbon model

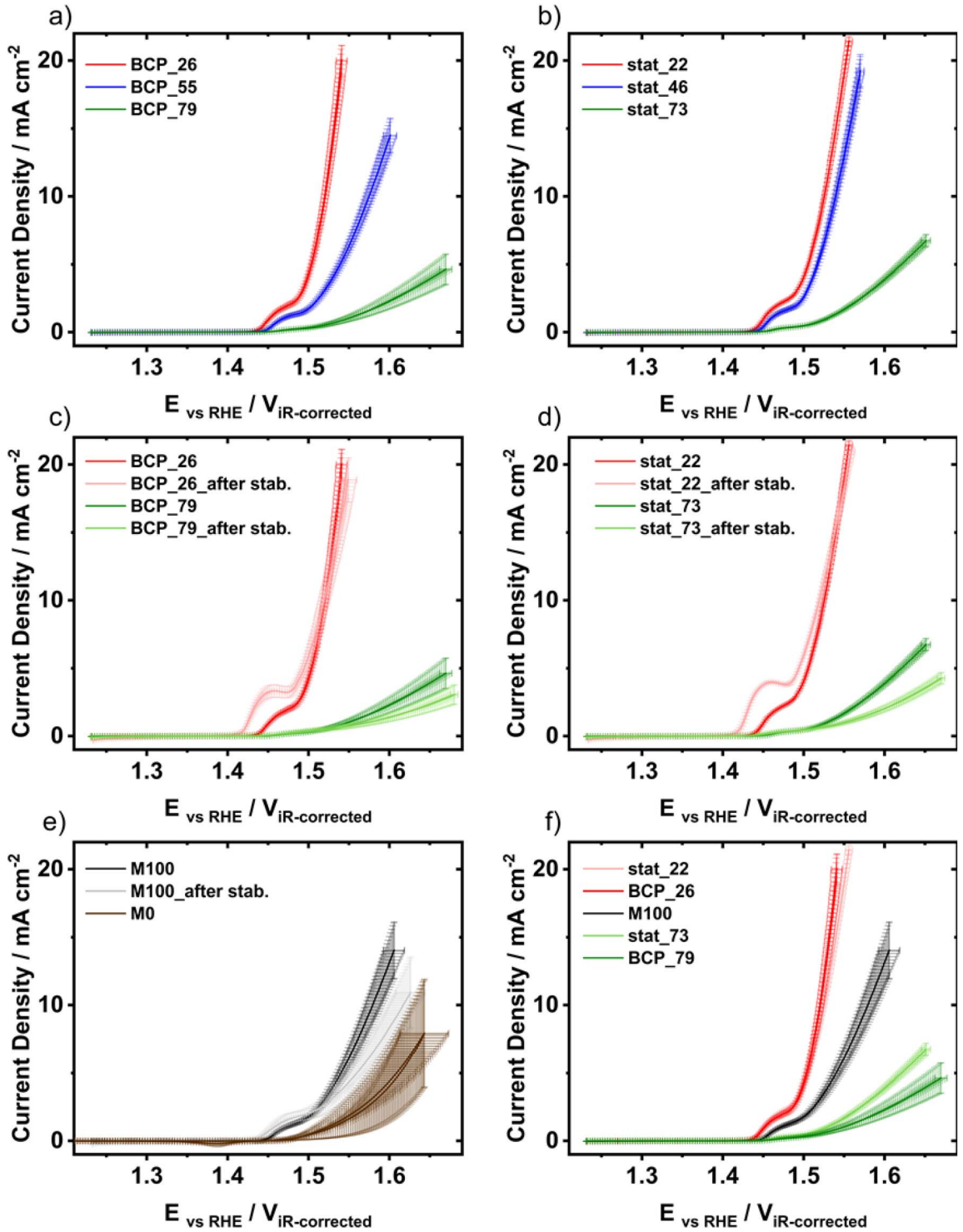

Fig. 6 OER activities for block (a) and statistical copolymers (b) as binders in RDE with NiFe-LDH catalyst in 0.1 M KOH solution. OER activities for block (c) and statistical copolymers (d) M0 and M100 (e) as binders in RDE before and after stability test. Comparison of OER activities of block and statistical copolymers as well as M100 (f).

electrodes with Nafion as binder, for which an increasing relative humidity led to increased electrical resistance.[61]

In our case, humidity is not varied within one experiment but the hydration level increases from BCP_26 to BCP_55 to BCP_79. Interestingly, stat_22 has an even lower IEC than BCP_26 but slightly inferior performance, suggesting that the trend of lowering IEC to improve RDE performance did not continue further. To further evaluate the properties of the prepared copolymers, AEMWE single cell measurements at 80 °C in 1 M KOH with a 5 cm^2 active area were conducted. All cells

were prepared identically *via* direct bar coating,[62] with only the binder being varied in the anode catalyst layer. For the cathode, commercial Pt/C catalyst on carbon paper was used with PiperION-A binder. For anode fabrication, the same NiFe-LDH catalyst as used as for the RDE measurements. Commercial PiperION-A, similar to M0, was selected as membrane and cathode binder, as well as for a reference anode binder system. Fig. 7 displays the cell voltage, high frequency resistance (HFR), and *iR*-corrected cell voltage. All single cells with copolymer binders in the anode exhibited either a similar or improved cell performance compared to the PiperION-A reference (Fig. 7 a, c, d, and f). The BCP series (Fig. 7a and c) showed a clearer distinction between each polymer. Here, the cell voltage obtained from the most hydrophilic BCP_79 was similar as for the PiperION-A reference and decreased with increasing IEC of the BCP binder. In the cell with the best performing BCP_26 a high

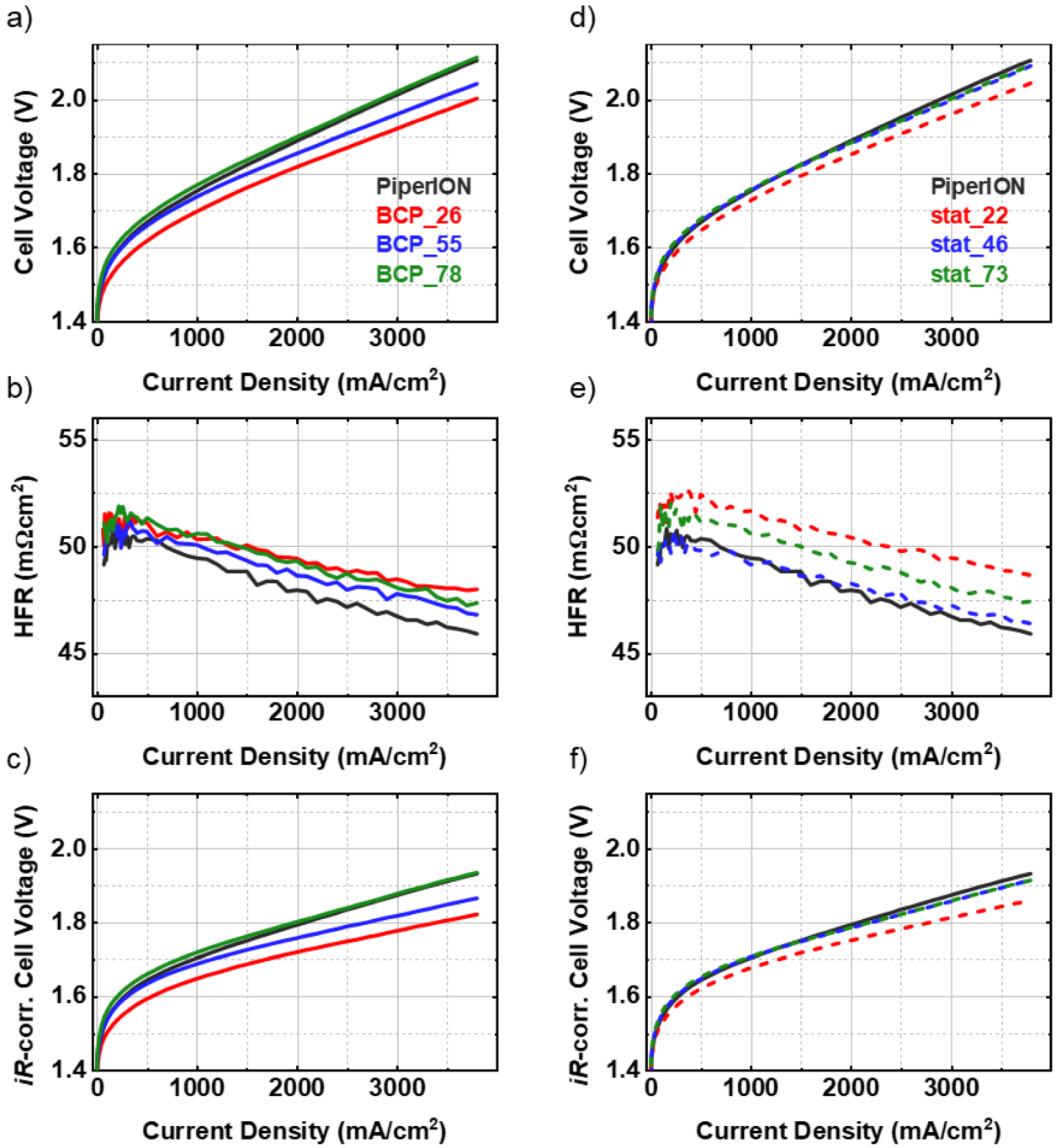

Fig. 7 Polarization curves and high frequency resistance of single cells with various block (a–c) and statistical copolymers (d–f) with various hydrophilic repeating units. The AEMWE cells were measured at 80 °C in 1 M KOH, 5 cm^2 cell area, PiperION A 40 μm membrane, NiFe-LDH anode catalyst loading 1.0 ± 0.1 mg cm^{-2}, Pt/C cathode 0.4 ± 0.05 mg cm^{-2}.

current density of 3800 mA cm^{-2} at 2 V was achieved. Notably, few reports have shown significantly better performance with NiFe-based anodes.[57,63–65] Compared to the device with PiperION-A as binder, the voltage of this cell was lowered by 50 mV at 1 A cm^{-2} and by 100 mV at 3 A cm^{-2}. The differences among the cells prepared with the stat binders were minor, but also in this case the most hydrophobic stat_22 binder consistently outperformed the cells with more hydrophilic stat_46 and stat_73. However, BCP_26 delivered the overall best performance and a reduction of the cell voltage of 40 mV at 3 A cm^{-2} compared to stat_22.

The HFR of all cells (Fig. 7b,e) remained consistent in the range of 50 mΩ cm^2, decreasing slightly with increasing current density. The minimal variation in HFR between the cells was in the range of reproducibility observed from previous measurements,[66] indicating that the HFR is mostly dominated by the membrane and less influenced by the catalyst layer including the binder. Thus, the improvement of the cell voltage by lowering the IEC of the binder is not due to ohmic resistance of the entire MEA rather than due to improved catalyst utilization in the less swollen anode layers, which in turn is caused by the better connectivity of catalyst particles and the resulting increased electrical conductivity. This is further corroborated by the kinetic analysis of the single cell data, where the cell with BCP_26 shows an up to 20% lower Tafel slope (Fig. S15). The significant increase in performance highlights the important role of the catalyst/binder layer for efficient operation, as already known from PEM water electrolysis and fuel cells.[67,68]

The results from single cell testing correlated well with the trends of the RDE measurements, confirming that RDE is well-suited for straightforward catalyst and binder screening.[35] With a metal loading of about 1 $\pm$ 0.1 mg cm^{-2}, the anode layer in an operational cell is typically ~5–10 μm[62] and hence much thicker compared to the RDE layers (<1 μm). Consequently, the hydroxide conductivity of the binder is expected to be less important in a thin RDE layer compared to a thicker catalyst layer in the MEA of a single cell. This can be a further reason why the largely different RDE activities within the series of BCPs did not fully translate to the single cell level. The same argumentation explains why BCP_26 and stat_22 show very similar RDE performance but BCP_26 with significantly better hydroxide conductivity outperforms stat_22 at the single cell level (reduction of cell voltage by 40 mV at 3 A cm^{-2}). Besides this, the overall low water uptake of both BCP_26 and stat_22 appears to be a major factor for the increase in performance in both cases.

From these results we identify the IEC as one of the most important parameters of an anode ionomer binder for AEMWE. Lowering the IEC strongly lowered WU, which is additionally almost temperature-independent for BCP_26. The low water content and resulting low swelling enabled an increase in electrical conductivity within the catalyst layer. Similar effects have been reported for the humidity-dependent electrical conductivity of a Pt/C/Nafion model electrode[34] and the catalyst-loading-dependent electrical conductivity of platinum group metal-free anodes.[69] In our work, the low hydration of BCP_26 led to increased catalyst utilization and in turn improved RDE and single cell performance. At this point the question of the existence of an ideal IEC arises, for which binder performance can be maximized. Efforts to use a BCP with an even lower IEC of 0.35 meq. g^{-1} as well as an entirely hydrophobic binder were unsuccessful due to altered solubility and incompatibility with the herein used protocols for MEA preparation (see Fig. S16 and S17). Also, the question of percolation of hydrophilic domains for fractions lower than 25% is questionable, which would deteriorate ionic transport. While hydroxide transport may not be the most important parameter for a binder, we note that a beneficial contribution of decent hydroxide transport can't be excluded neither. Nevertheless, in light of the binder stabilities reported in Fig. S14, further investigation of entirely hydrophobic binders[70] appears promising.

Regarding the relationship between hydroxide conductivity, WU and performance of BCPs for AEMWE in general, it is obvious that BCP_26 features an almost ideal set of characteristics for membrane applications, provided that hydrolytic stability can be improved. This is particularly important at low hydration, where nucleophilicity of the hydroxide anion is increased.[53] Further studies along these lines are underway, and cations even more stable than dimethyl piperidinium are in the spotlight.[54–56,58,59]

Conclusions

In conclusion, we have designed, synthesized and characterized a series of block copolymers in a one pot polyhydroxyalkylation reaction and used them as binder ionomers in anode layers for AEMWE. The block copolymers carry poly(biphenyl piperidinium) blocks as hydrophilic segments and hydrophobic ones based on *meta*-terphenyl and trifluoroacetophenone. The reaction design allowed to modulate the ion exchange capacity within a broad range of 0.94–2.68 meq. g^{-1}. An in-depth comparison with statistical copolymer analogs strongly suggests that monomer scrambling occurs during the synthesis of the second block, leading to partial fragmentation. The synthesis of the statistical analogs is characterized by segmentation, such that overall (i) the synthesis of block copolymers is complex and (ii) the final chain architecture of block and statistical copolymers is less different than one would expect in the absence of fragmentation and segmentation. While water uptake and swelling of the block copolymers correlated with fractions of hydrophilic monomers, the hydroxide conductivity was highest for the block copolymer BCP_26 (174 mS cm^{-1} at 80 °C) with only 26 wt-% of hydrophilic poly(biphenyl piperidinium) corresponding to the lowest ion exchange capacity of 0.94 meq. g^{-1} among the BCP series. The same BCP_26 also exhibited a low, almost temperature-independent water uptake that we ascribe to the small hydrophilic weight fraction and the ability of the hydrophobic block to order. However, the low hydration level of BCP_26 also led to faster hydrolytic degradation of piperidinium, highlighting the necessity to consider hydration level-dependent hydroxide stability as well as the use of alternative, more stable cations, particularly when low hydration conditions are envisaged. Finally, this block copolymer binder also delivered the highest current density and

stability in RDE experiments. The superior RDE performance of this same BCP was attributed to the low ion exchange capacity, low water uptake and swelling, leading to enhanced electrical conductivity between non-precious metal NiFe-LDH catalyst particles and, as a result, enhanced catalyst utilization. RDE also proved to be an excellent predictor for single cell testing, where BCP_26 yielded a high current density of 3800 mA cm^{-2} at 2 V (non-IR-corrected) and outperformed all other binder materials tested herein, including statistical copolymers as well as well-established and commercially AEM materials. Overall, this work has provided various design criteria for anode binders that significantly impact anode performance.

Author contributions

Richard Weber: investigation, methodology, validation, writing – original draft. Malte Klingenhof: investigation, methodology, validation, writing – review & editing. Oleksandr Dolynchuk: investigation, methodology, validation, writing – review & editing. Luis Hagner: investigation, methodology, validation, writing – review & editing. Lukas Metzler: investigation, methodology, validation, writing – review & editing. Susanne Koch: methodology, validation, funding acquisition, writing – review & editing. Mario Zerson: investigation, methodology, visualization, validation, writing – review & editing. Robert Magerle: investigation, methodology, visualization, validation, conceptualization, supervision, writing – review & editing. Peter Strasser: conceptualization, funding acquisition, supervision. Severin Vierrath: conceptualization, funding acquisition, supervision. Michael Sommer: conceptualization, funding acquisition, supervision, writing – review & editing.

Conflicts of interest

There are no conflicts to declare.

Data availability

The data supporting this article has been published in form of an supplementary information (SI), containing details on polymer synthesis and characterization, MEA preparation and additional electrochemical characterization. Supplementary information is available. See DOI: https://doi.org/10.1039/d6ta00653a.

Acknowledgements

Funding from the BMBF (AEMready, Grant No. 03SF0613A) is greatly acknowledged. O.D. acknowledges financial support from the Ministry of Science, Energy, Climate Protection and Environment of the State of Saxony-Anhalt (grant no. 41-04032/2018).

Notes and references

1 H. A. Miller, K. Bouzek, J. Hnat, S. Loos, C. I. Bernäcker, T. Weißgärber, L. Röntzsch and J. Meier-Haack, *Sustain. Energy Fuels*, 2020, **4**, 2114–2133.
2 K. Ayers, N. Danilovic, R. Ouimet, M. Carmo, B. Pivovar and M. Bornstein, *Annu. Rev. Chem. Biomol. Eng.*, 2019, **10**, 219–239.
3 D. Li, A. R. Motz, C. Bae, C. Fujimoto, G. Yang, F.-Y. Zhang, K. E. Ayers and Y. S. Kim, *Energy Environ. Sci.*, 2021, **14**, 3393–3419.
4 A. Buttler and H. Spliethoff, *Renew. Sustain. Energy Rev.*, 2018, **82**, 2440–2454.
5 A. Y. Faid and S. Sunde, *Energy Technol.*, 2022, **10**, 2200506.
6 R. Abbasi, B. P. Setzler, S. Lin, J. Wang, Y. Zhao, H. Xu, B. Pivovar, B. Tian, X. Chen, G. Wu and Y. Yan, *Adv. Mater.*, 2019, **31**, 1805876.
7 D. S. Kim, C. Welch, R. P. Hjelm, Y. S. Kim and M. D. Guiver, in *Polymer Science: A Comprehensive Reference*, eds. K. Matyjaszewski and M. Möller, Elsevier, Amsterdam, 2012, pp. 691–720.
8 P. Mardle, B. Chen and S. Holdcroft, *ACS Energy Lett.*, 2023, **8**, 3330–3342.
9 I. Wu, K. C. Dunn, J. W. Creel, A. N. Radzanowski, K. J. Beiler, M. S. Ezell, A. M. Johnson, D. J. Carmosino, M. J. Salgado, C. Kim, M.-C. Kuo, N. C. Buggy, S. Seifert, E. B. Coughlin and A. M. Herring, *ACS Appl. Polym. Mater.*, 2023, **5**, 5834–5845.
10 J. H. Hsu, C. R. Peltier, M. Treichel, J. C. Gaitor, Q. Li, R. Girbau, A. J. Macbeth, H. D. Abruña, K. J. T. Noonan, G. W. Coates and B. P. Fors, *Angew. Chem.*, 2023, **135**, e202304778.
11 D. Li, E. J. Park, W. Zhu, Q. Shi, Y. Zhou, H. Tian, Y. Lin, A. Serov, B. Zulevi, E. D. Baca, C. Fujimoto, H. T. Chung and Y. S. Kim, *Nat. Energy*, 2020, **5**, 378–385.
12 A. R. Motz, D. Li, A. Keane, L. D. Manriquez, E. J. Park, S. Maurya, H. Chung, C. Fujimoto, J. Jeon, M. K. Pagels, C. Bae, K. E. Ayers and Y. S. Kim, *J. Mater. Chem. A*, 2021, **9**, 22670–22683.
13 L. Xiao, S. Zhang, J. Pan, C. Yang, M. He, L. Zhuang and J. Lu, *Energy Environ. Sci.*, 2012, **5**, 7869–7871.
14 J. Pan, Y. Li, L. Zhuang and J. Lu, *Chem. Commun.*, 2010, **46**, 8597–8599.
15 J. Parrondo, C. G. Arges, M. Niedzwiecki, E. B. Anderson, K. E. Ayers and V. Ramani, *RSC Adv.*, 2014, **4**, 9875–9879.
16 Y. Leng, G. Chen, A. J. Mendoza, T. B. Tighe, M. A. Hickner and C.-Y. Wang, *J. Am. Chem. Soc.*, 2012, **134**, 9054–9057.
17 C. Busacca, S. C. Zignani, A. Di Blasi, O. Di Blasi, M. Lo Faro, V. Antonucci and A. S. Aricò, *Int. J. Hydrogen Energy*, 2019, **44**, 20987–20996.
18 D. Xu, M. B. Stevens, M. R. Cosby, S. Z. Oener, A. M. Smith, L. J. Enman, K. E. Ayers, C. B. Capuano, J. N. Renner, N. Danilovic, Y. Li, H. Wang, Q. Zhang and S. W. Boettcher, *ACS Catal.*, 2019, **9**, 7–15.

19 S. Koch, P. A. Heizmann, S. K. Kilian, B. Britton, S. Holdcroft, M. Breitwieser and S. Vierrath, *J. Mater. Chem. A*, 2021, **9**, 15744–15754.
20 B. Chen, P. Mardle and S. Holdcroft, *J. Power Sources*, 2022, **550**, 232134.
21 R. A. Krivina, G. A. Lindquist, M. C. Yang, A. K. Cook, C. H. Hendon, A. R. Motz, C. Capuano, K. E. Ayers, J. E. Hutchison and S. W. Boettcher, *ACS Appl. Mater. Interfaces*, 2022, **14**, 18261–18274.
22 N. Chen, S. Yane Paek, J. Yeon Lee, J. Hyeong Park, S. Young Lee and Y. Moo Lee, *Energy Environ. Sci.*, 2021, **14**, 6338–6348.
23 G. A. Lindquist, S. Z. Oener, R. Krivina, A. R. Motz, A. Keane, C. Capuano, K. E. Ayers and S. W. Boettcher, *ACS Appl. Mater. Interfaces*, 2021, **13**, 51917–51924.
24 P. M. Bakvand, D. Pan, A. Allushi and P. Jannasch, *Adv. Energy Mater.*, 2024, 2402869.
25 H. Koshikawa, H. Murase, T. Hayashi, K. Nakajima, H. Mashiko, S. Shiraishi and Y. Tsuji, *ACS Catal.*, 2020, **10**, 1886–1893.
26 D. Chanda, J. Hnát, T. Bystron, M. Paidar and K. Bouzek, *J. Power Sources*, 2017, **347**, 247–258.
27 D. Chanda and S. Basu, *Int. J. Hydrogen Energy*, 2018, **43**, 21999–22011.
28 R. A. Tufa, E. Rugiero, D. Chanda, J. Hnàt, W. van Baak, J. Veerman, E. Fontananova, G. Di Profio, E. Drioli, K. Bouzek and E. Curcio, *J. Membr. Sci.*, 2016, **514**, 155–164.
29 Y. S. Kim, *Adv. Sci.*, 2023, **10**, 2303914.
30 F. Liu, K. Miyatake, M. Tanabe, A. M. A. Mahmoud, V. Yadav, L. Guo, C. Y. Wong, F. Xian, T. Iwataki, M. Uchida and K. Kakinuma, *Adv. Sci.*, 2024, **11**, 2402969.
31 I. Matanovic, S. Maurya, E. J. Park, J. Y. Jeon, C. Bae and Y. S. Kim, *Chem. Mater.*, 2019, **31**, 4195–4204.
32 N. Du, C. Roy, R. Peach, M. Turnbull, S. Thiele and C. Bock, *Chem. Rev.*, 2022, **122**, 11830–11895.
33 N. Chen and Y. M. Lee, *Prog. Polym. Sci.*, 2021, **113**, 101345.
34 D. R. P. Morris, S. P. Liu, D. Villegas Gonzalez and J. T. Gostick, *ACS Appl. Mater. Interfaces*, 2014, **6**, 18609–18618.
35 R. Weber, M. Klingenhof, S. Koch, L. Metzler, T. Merzdorf, J. Meier-Haack, P. Strasser, S. Vierrath and M. Sommer, *J. Mater. Chem. A*, 2024, **12**, 7826–7836.
36 R. Gentile, S. C. Zignani, M. Zatoń, M. Dupont, F. Lecœur, N. Donzel, A. Amel, E. Tal-Gutelmacher, A. Salanitro, A. S. Aricó, S. Cavaliere, D. J. Jones and J. Rozière, *ChemSusChem*, 2024, e202400825.
37 G. Xu, J. Pan, X. Zou, Z. Jin, J. Zhang, P. Fang, Q. Zhang, Z. Sun and F. Yan, *Adv. Funct. Mater.*, 2023, **33**, 2302364.
38 X. Wu, N. Chen, H.-A. Klok, Y. M. Lee and X. Hu, *Angew. Chem., Int. Ed.*, 2022, **61**, e202114892.
39 L. Zhu, J. Pan, Y. Wang, J. Han, L. Zhuang and M. A. Hickner, *Macromolecules*, 2016, **49**, 815–824.
40 G. Deng, Y. Liao, Y. Lin, L. Ding and H. Wang, *Angew. Chem., Int. Ed.*, 2024, **63**, e202412632.
41 L. Hager, T. Maron, T. Ngo Thanh, J. Stonawski, A. Hutzler, T. Böhm, P. Strasser, S. Thiele and J. Kerres, *J. Mater. Chem. A*, 2025, **13**, 8059–8074.
42 A. Allushi, P. M. Bakvand, H. Gong and P. Jannasch, *Mater. Adv.*, 2023, **4**, 3733–3745.
43 R. Selhorst, J. Gaitor, M. Lee, D. Markovich, Y. Yu, M. Treichel, C. Olavarria Gallegos, T. Kowalewski, L. F. Kourkoutis, R. C. Hayward and K. J. T. Noonan, *ACS Appl. Energy Mater.*, 2021, **4**, 10273–10279.
44 Y. Ma, C. Hu, G. Yi, Z. Jiang, X. Su, Q. Liu, J. Y. Lee, S. Y. Lee, Y. M. Lee and Q. Zhang, *Angew. Chem., Int. Ed.*, 2023, **62**, e202311509.
45 J. S. Olsson, T. H. Pham and P. Jannasch, *Adv. Funct. Mater.*, 2018, **28**, 1702758.
46 W.-H. Lee, E. J. Park, J. Han, D. W. Shin, Y. S. Kim and C. Bae, *ACS Macro Lett.*, 2017, **6**, 566–570.
47 C. Long, Z. Wang and H. Zhu, *Int. J. Hydrogen Energy*, 2021, **46**, 18524–18533.
48 K.-D. Kreuer and G. Portale, *Adv. Funct. Mater.*, 2013, **23**, 5390–5397.
49 P. Toudret, J. Wolanin, G. Gebel and A. Morin, *J. Power Sources*, 2023, **586**, 233671.
50 I. W. Hamley and V. Castelletto, *Prog. Polym. Sci.*, 2004, **29**, 909–948.
51 M. Farcasiu, T. R. Forbus and B. R. Rubin, *Energy Fuels*, 1987, **1**, 28–31.
52 M. Mandal, G. Huang, N. U. Hassan, W. E. Mustain and P. A. Kohl, *J. Mater. Chem. A*, 2020, **8**, 17568–17578.
53 D. R. Dekel, M. Amar, S. Willdorf, M. Kosa, S. Dhara and C. E. Diesendruck, *Chem. Mater.*, 2017, **29**, 4425–4431.
54 J. Fan, S. Willdorf-Cohen, E. M. Schibli, Z. Paula, W. Li, T. J. G. Skalski, A. T. Sergeenko, A. Hohenadel, B. J. Frisken, E. Magliocca, W. E. Mustain, C. E. Diesendruck, D. R. Dekel and S. Holdcroft, *Nat. Commun.*, 2019, **10**, 2306.
55 A. Allushi, T. H. Pham, J. S. Olsson and P. Jannasch, *J. Mater. Chem. A*, 2019, **7**, 27164–27174.
56 P. M. Bakvand and P. Jannasch, *J. Membr. Sci.*, 2025, **717**, 123656.
57 L. Yin, R. Ren, L. He, W. Zheng, Y. Guo, L. Wang, H. Lee, J. Du, Z. Li, T. Tang, G. Ding and L. Sun, *Angew. Chem., Int. Ed.*, 2024, **63**, e202400764.
58 W. Zou, G. Tang, K. Peng, X. Mo, T. Hu, Z. Yang and T. Xu, *Angew. Chem., Int. Ed.*, 2025, **64**, e202514264.
59 Q. Zhang, R. Ren, L. Yin and L. Sun, *Chem.–Eur. J.*, 2025, **31**, e202404264.
60 H. A. El-Sayed, A. Weiß, L. F. Olbrich, G. P. Putro and H. A. Gasteiger, *J. Electrochem. Soc.*, 2019, **166**, F458–F464.
61 D. R. P. Morris, S. P. Liu, D. Villegas Gonzalez and J. T. Gostick, *ACS Appl. Mater. Interfaces*, 2014, **6**, 18609–18618.
62 S. Koch, L. Metzler, S. K. Kilian, P. A. Heizmann, F. Lombeck, M. Breitwieser and S. Vierrath, *Adv. Sustain. Syst.*, 2023, **7**, 2200332.
63 D. Li, E. J. Park, W. Zhu, Q. Shi, Y. Zhou, H. Tian, Y. Lin, A. Serov, B. Zulevi, E. D. Baca, C. Fujimoto, H. T. Chung and Y. S. Kim, *Nat. Energy*, 2020, **5**, 378–385.
64 M. S. Cha, J. E. Park, S. Kim, S.-H. Shin, S. H. Yang, S. J. Lee, T.-H. Kim, D. M. Yu, S. So, K. M. Oh, Y.-E. Sung, Y.-H. Cho and J. Y. Lee, *J. Mater. Chem. A*, 2022, **10**, 9693–9706.

65 H. S. Kwon, J. Byeon, C. Lim, J. Park, J. Lee, J. Choi, T. H. Kim, J. Lee and B. J. Kim, *Adv. Funct. Mater.*, 2026, **36**, e17390.
66 M. Klingenhof, H. Trzesniowski, S. Koch, J. Zhu, Z. Zeng, L. Metzler, A. Klinger, M. Elshamy, F. Lehmann, P. W. Buchheister, A. Weisser, G. Schmid, S. Vierrath, F. Dionigi and P. Strasser, *Nat. Catal.*, 2024, **7**, 1213–1222.
67 T. Schuler, J. M. Ciccone, B. Krentscher, F. Marone, C. Peter, T. J. Schmidt and F. N. Büchi, *Adv. Energy Mater.*, 2020, **10**, 1903216.
68 H. Liepold, A. Bird, P. A. Heizmann, H. Fadlullah, H. Nguyen, C. Klose, S. Holdcroft, A. Kusoglu, S. Vierrath and A. Münchinger, *J. Power Sources*, 2024, **624**, 235537.
69 M. E. Kreider, H. Yu, L. Osmieri, M. R. Parimuha, K. S. Reeves, D. H. Marin, R. T. Hannagan, E. K. Volk, T. F. Jaramillo, J. L. Young, P. Zelenay and S. M. Alia, *ACS Catal.*, 2024, **14**, 10806–10819.
70 H. Lim, N. I. Kim, G. Shin, J. Lee, S. Kim, S.-W. Myeong, C. Kim, S. M. Choi and T. Park, *Adv. Energy Mater.*, 2025, **15**, 2501038.